Mechanisms Driving the Time-Dependent Salt Flux in a Partially Stratified Estuary*

JAMES A. LERCZAK AND W. ROCKWELL GEYER

Woods Hole Oceanographic Institution, Woods Hole, Massachusetts

ROBERT J. CHANT

Institute of Marine and Coastal Science, Rutgers, The State University of New Jersey, New Brunswick, New Jersey

(Manuscript received 29 November 2004, in final form 13 March 2006)

ABSTRACT

The subtidal salt balance and the mechanisms driving the downgradient salt flux in the Hudson River estuary are investigated using measurements from a cross-channel mooring array of current meters, temperature and conductivity sensors, and cross-channel and along-estuary shipboard surveys obtained during the spring of 2002. Steady (subtidal) vertical shear dispersion, resulting from the estuarine exchange flow, was the dominant mechanism driving the downgradient salt flux, and varied by over an order of magnitude over the spring–neap cycle, with maximum values during neap tides and minimum values during spring tides. Corresponding longitudinal dispersion rates were as big as 2500 $m^2 s^{-1}$ during neap tides. The salinity intrusion was not in a steady balance during the study period. During spring tides, the oceanward advective salt flux resulting from the net outflow balanced the time rate of change of salt content landward of the study site, and salt was flushed out of the estuary. During neap tides, the landward steady shear dispersion salt flux exceeded the oceanward advective salt flux, and salt entered the estuary. Factor-of-4 variations in the salt content occurred at the spring–neap time scale and at the time scale of variations in the net outflow. On average, the salt flux resulting from tidal correlations between currents and salinity (tidal oscillatory salt flux) was an order of magnitude smaller than that resulting from steady shear dispersion. During neap tides, this flux was minimal (or slightly countergradient) and was due to correlations between tidal currents and vertical excursions of the halocline. During spring tides, the tidal oscillatory salt flux was driven primarily by oscillatory shear dispersion, with an associated longitudinal dispersion rate of about 130 $m^2 s^{-1}$.

1. Introduction

The salinity intrusion in an estuary is maintained by a competition between two opposing longitudinal salt fluxes—an advective flux resulting from freshwater outflow, tending to drive salt out of the estuary; and a downgradient[1] salt flux, tending to drive salt landward. The dispersion rate associated with the downgradient flux can vary by two orders of magnitude in different estuaries, from ~10 to 1000 $m^2 s^{-1}$ (Fischer et al. 1979; Geyer and Signell 1992), depending on the underlying physical mechanisms driving the flux. This dispersion rate sets the residence time of waterborne materials in estuaries, including sediments and pollutants; controls how far the salinity intrusion advances upriver; and sets the response time of an estuary to changes in forcing. Determining the mechanisms that drive the downgradient salt flux in different estuarine classes, therefore, is a fundamental objective in estuarine research.

The tidally averaged advective and downgradient salt fluxes are notoriously difficult to measure, for several reasons (Jay et al. 1997; Simpson et al. 2001; Bowen and Geyer 2003). The amplitude of the fluctuating component of the instantaneous salt flux, due primarily to tidal advection of the mean along-channel salinity gradient, can exceed the tidally averaged salt flux by an order of magnitude or more. Small errors or biases in

[1] Consistent with common usage, we refer to fluxes from high salinity to low salinity, that is, in the same direction as Fickian diffusion as downgradient fluxes. Fluxes from low salinity to high salinity are referred to as countergradient fluxes.

* Woods Hole Oceanographic Institution Contribution Number 11272.

Corresponding author address: James A. Lerczak, Department of Physical Oceanography, MS #21, Woods Hole Oceanographic Institution, Woods Hole, MA 02543.
E-mail: jlerczak@whoi.edu

measuring the instantaneous salt flux, therefore, can lead to large errors in the estimate of the tidally averaged, cross-sectionally integrated salt flux $\mathcal{F}_S$. The salinity and current fields have both cross-channel and vertical structure, and it is important to capture this spatial structure in order to obtain an accurate estimate of $\mathcal{F}_S$ (Bowen and Geyer 2003). Time series profiles of currents and salinity at a single cross-estuary location, thus, may result in erroneous estimates of the advective and downgradient salt fluxes.

Field studies to calculate the advective and downgradient salt fluxes in different estuaries have been conducted by several investigators. Many involve measurements of currents and salinity across a channel cross section to directly calculate $\mathcal{F}_S$ (Hughes and Rattray 1980; Hunkins 1981; Uncles et al. 1985; Dronkers and van de Kreeke 1986; Jay and Smith 1990; Kay et al. 1996; Geyer and Nepf 1996). In these studies, current and salinity fields were decomposed spatially and temporally to separate the downgradient and advective components of $\mathcal{F}_S$ and identify the mechanisms responsible for the downgradient salt flux. Other studies have decomposed $\mathcal{F}_S$ based on vertical measurements of current and salinity at one location in an estuarine cross section with the effect of lateral variability inferred from more limited measurements or from numerical modeling (Simpson et al. 2001; Bowen and Geyer 2003). The length of time series used in most studies ranged from a single semidiurnal tidal cycle to several days, giving only limited information about the variations in the amplitude of the downgradient salt flux and the dominant dispersion mechanisms at work under different forcing conditions. An exception is the study of Bowen and Geyer (2003), for which the salt flux and its components were calculated at a cross section in the Hudson River estuary for a period of 70 days during the summer and autumn of 1995.

Here, we estimate the downgradient salt flux and determine the salt balance at a channel cross section of the Hudson River estuary using measurements from a cross-channel mooring array of current meters, temperature and conductivity sensors, and cross-channel and along-estuary shipboard surveys obtained during the spring of 2002. The goals of this study are to 1) estimate the downgradient salt flux and determine how its magnitude varies with changes in forcing, 2) determine the mechanisms that contribute most significantly to the downgradient salt flux under different forcing conditions, and 3) determine the salt balance within the estuary under different forcing conditions. We extend the salt flux investigations of Bowen and Geyer (2003) in two ways. First, we directly measure the cross-sectional spatial structure of the various components of $\mathcal{F}_S$, unlike Bowen and Geyer (2003), who inferred the lateral structure using a numerical model. Second, we measure the salt flux during a time period when buoyancy forcing resulting from the freshwater outflow was large in amplitude and variable in time, in contrast to Bowen and Geyer (2003), for which the buoyancy forcing was weak because of a drought throughout most of their study period, with the exception of a storm at the end of their field deployment.

2. Mechanisms driving the downgradient salt flux

The one-dimensional, along-estuary salt conservation equation is often cast in the following form (Harleman and Thatcher 1974; Kranenburg 1986; Monismith et al. 2002):

$$A_o(x)\frac{\partial S_o}{\partial t} = \frac{\partial}{\partial x}\left[Q_f S_o + A_o(x)K(x)\frac{\partial S_o}{\partial x}\right], \qquad (1)$$

where A_o is the tidally averaged, cross-sectional area, x is the along-estuary distance increasing in the upstream direction, Q_f is the net outflow, S_o is the cross-sectional average salinity, and K is the along-estuary dispersion rate. By convention, Q_f is positive when it flows toward the ocean. In the steady state, the oceanward advective flux $-Q_f S_o$ is balanced by a landward, downgradient flux. The essential physics that drives the downgradient salt flux is distilled into the dispersion rate, and the challenge is to understand the dynamics that set the value of K for a particular estuary under varying forcing conditions.

Various mechanisms may be responsible for the downgradient flux of salt in estuaries. Here, we distinguish between *steady shear dispersion* (Taylor 1953), resulting from the combination of straining the salinity field by vertically or laterally sheared subtidal currents and vertical or lateral mixing, and *tidal oscillatory salt flux*, resulting from tidal correlations between longitudinal currents and salinity variability.

a. Steady shear dispersion

The estuarine exchange flow draws salty water up estuary near the bottom of the channel and advects comparatively fresh water oceanward near the surface, resulting in a net downgradient salt flux $\mathcal{F}_\varepsilon$. For the steady-state solution of Hansen and Rattray (1965), which assumes a vertically sheared exchange flow driven by an along-estuary baroclinic pressure gradient balanced by vertical mixing of momentum and salt in a rectangular channel, $\mathcal{F}_\varepsilon$ is given by

$$\mathcal{F}_{\varepsilon_{\mathrm{HR}}} = -A_o\alpha\frac{(g\beta)^2H^8}{\kappa_v\nu_v^2}\left|\frac{\partial S_o}{\partial x}\right|^2\frac{\partial S_o}{\partial x} \equiv -A_oK_{\mathrm{HR}}\frac{\partial S_o}{\partial x}, \qquad (2)$$

where α is a constant ($\approx 1.3 \times 10^{-5}$), g is the gravitational acceleration, β is the coefficient of saline expansion, H is the depth of the water column, and κ_v and ν_v are the constant vertical eddy diffusivity and viscosity, respectively. Because salinity is dynamically active in driving the estuarine exchange flow, the dispersion rate differs from that for vertical shear dispersion of a passive tracer, which depends inversely on the vertical eddy diffusivity (Taylor 1953). For the Hansen and Rattray solution, K_{HR} is inversely proportional to the cube of κ_v (assuming that $\kappa_v \sim \nu_v$), and one would, therefore, predict a strong inverse dependence of $\mathcal{F}_\varepsilon$ on the strength of tidally generated mixing. Further, K_{HR} is proportional to the square of the longitudinal salinity gradient, and, therefore, depends sensitively on the length of the salinity intrusion.

While Eq. (2) offers some insight into the dependence of $\mathcal{F}_\varepsilon$ on tidal mixing and Q_f, dynamics that may be important to particular estuaries are missing or obscured in the formulation. For example, in wide weakly stratified estuaries or estuaries with large lateral bathymetric variation, lateral variations in salinity and in the subtidal longitudinal circulation may dominate over vertical variations. For such estuaries, lateral steady shear dispersion may dominate over vertical shear dispersion (Fischer 1972; Smith 1976), and the lateral mixing rate, and, consequently, the longitudinal shear dispersion rate, is set by the strength and structure of the tidal and subtidal lateral circulation in the estuary, which controls lateral exchange (Smith 1976).

The potential dependence of mixing on Q_f is not explicit in the Hansen and Rattray (1965) formulation. Monismith et al. (2002) suggest that an increase in Q_f increases stratification in the northern San Francisco Bay estuary, which, in turn, suppresses vertical mixing and increases $\mathcal{F}_\varepsilon$. This dependence of mixing on Q_f results in a much weaker dependence of the length of the salinity intrusion on Q_f than that predicted by Hansen and Rattray (1965).

Other mechanisms, may be important to driving the sheared, subtidal longitudinal circulation that are not explicitly taken in account by (2), such as tidal rectification (Li and O'Donnell 1997), tidal asymmetries in the lateral advection of tidal currents (Lerczak and Geyer 2004), and tidal asymmetries in vertical mixing (Jay and Musiak 1996; Stacey et al. 2001).

b. Tidal oscillatory salt flux

While tidal oscillations in along-channel currents and salinity temporally average to zero, temporal correlations between the two can lead to a downgradient salt flux. Here we briefly discuss three mechanisms that drive these temporal correlations: tidal oscillatory shear dispersion, tidal trapping, and tidal pumping. More detailed descriptions are given by Fischer et al. (1979).

Vertical tidal oscillatory shear dispersion results from the straining and vertical mixing of the salinity field by vertically sheared oscillatory tidal currents (Okubo 1967; Larsen 1977; Fischer et al. 1979; Ou et al. 2000). The longitudinal dispersion rate associated with tidal oscillatory shear dispersion is maximal when the tidal period matches the vertical mixing time scale. For a homogeneous fluid, and assuming a linear vertical profile for the tidal velocity, the maximum horizontal dispersion rate resulting from vertical tidal oscillatory shear dispersion is given by (Zimmerman 1986)

$$\max(K_{\mathrm{VOSD}}) \approx 0.02 \frac{U_T^2}{\omega}, \tag{3}$$

where U_T is the tidal amplitude and ω is the tidal frequency. With this expression, the maximum dispersion rate resulting from the vertical tidal oscillatory shear dispersion is only $\sim 100\ \mathrm{m^2\ s^{-1}}$.

In estuaries with side embayments or large tidal flats, salt can be "stored" in the embayment or tidal flat during a particular phase of the tidal cycle and injected back into the main estuarine channel at a different phase of the tide, resulting in stirring of the salinity field and a downgradient salt flux referred to as tidal trapping (Okubo 1973; Fischer et al. 1979).

A tidal oscillatory salt flux can also occur in estuaries with longitudinal variations in bathymetry, such as near the mouth of an estuary, where flood–ebb asymmetries in the spatial structure of tidal currents exist (Stommel and Farmer 1952, chapters 3 and 4; Dronkers and van de Kreeke 1986; Chadwick and Largier 1999). This mechanism is often referred to as tidal pumping (Fischer et al. 1979; Simpson et al. 2001). Jay and Smith (1990) observed a tidal oscillatory salt flux in the Columbia River estuary that was comparable to or larger than steady shear dispersion, and was due to correlations between halocline fluctuations and tidal currents. Similarly, Geyer and Nepf (1996) found that tidal pumping observed in the Hudson estuary near a channel constriction could be explained by the distortion of the tidally averaged shear flow by tidal frequency vertical excursions of the halocline, caused by a hydraulic response to the constriction. They note that this mechanism should not be regarded as a dispersive flux, and they hypothesize that such a mechanism could lead to a countergradient flux in the vicinity of channel expansions.

The distinction between tidal trapping and tidal pumping is subtle. Formally, tidal trapping does not require longitudinal bathymetric variations and is determined by parameters local to a particular cross sec-

tion, for example, the ratio of the channel to the trap volume and the lateral exchange rate between the trap and the channel (Okubo 1973). In contrast, Dronkers and van de Kreeke (1986) refer to tidal pumping as a "nonlocal" salt flux, because it results from the distortion of the subtidal shear flow as it is advected longitudinally by tidal currents in regions of rapid variation in bathymetry. In practice, however, an objective framework for distinguishing between these mechanisms in realistic estuaries with complex longitudinal and lateral bathymetric variability is lacking.

3. Salt flux decomposition

To calculate the salt flux, we transform all variables to the following (λ, σ) coordinate system:

$$\lambda = y/B \quad \text{and} \quad \sigma = \frac{z - \xi(t)}{h(\lambda) + \xi(t)}, \tag{4}$$

where y and z are cross-channel and vertical coordinates, respectively, B is the breadth of the channel, h is the mean water depth at a particular cross-channel location, and ξ is sea level, which varies on tidal and subtidal time scales. The value of λ ranges from 0 to 1, while σ ranges from -1 to 0. In this coordinate system, the total salt flux $\mathcal{F}_S$ is given by

$$\mathcal{F}_S = \left\langle \int\int uS\, dA \right\rangle \left\langle \int_0^1 \int_{-1}^0 B(h + \xi) uS\, d\sigma\, d\lambda \right\rangle, \tag{5}$$

where the angled brackets indicate a low-pass, subtidal temporal filter (here, we use a filter with a half-amplitude at 33 h). To isolate the mechanisms contributing to the dispersive salt flux, we decompose both u and S into three components that are tidally and cross-sectionally averaged, tidally averaged and cross-sectionally varying, and tidally and cross-sectionally varying, according to

$$\phi_o = \frac{1}{A_o} \left\langle \int\int \phi(y, z, t)\, dA \right\rangle = \frac{1}{A_o} \left\langle \int_0^1 \int_{-1}^0 B(h + \xi)\phi\, d\sigma\, d\lambda \right\rangle, \tag{6}$$

$$\phi_\varepsilon(\lambda, \sigma) = \left\langle \frac{h + \xi}{h} \phi \right\rangle - \phi_o, \quad \text{and} \tag{7}$$

$$\phi_\mathcal{T}(\lambda, \sigma, t) = \phi - \phi_o - \phi_\varepsilon, \tag{8}$$

where ϕ refers to either u or S, and A_o is the low-passed cross-sectional area. The component $\phi_\mathcal{T}$ varies predominantly on tidal scales, while ϕ_o and ϕ_ε vary only on subtidal time scales. With this decomposition, the total salt flux is given by

$$\mathcal{F}_S = \left\langle \int_0^1 \int_{-1}^0 B(h + \xi)(u_o + u_\varepsilon + u_\mathcal{T})(S_o + S_\varepsilon + S_\mathcal{T})\, d\sigma\, d\lambda \right\rangle \approx \left\langle \int_0^1 \int_{-1}^0 B(h + \xi)(u_o S_o + u_\varepsilon S_\varepsilon + u_\mathcal{T} S_\mathcal{T})\, d\sigma\, d\lambda \right\rangle \equiv -Q_f S_o + \mathcal{F}_\varepsilon + \mathcal{F}_\mathcal{T}, \tag{9}$$

where $\mathcal{F}_\varepsilon$ is the salt flux resulting from steady shear dispersion and $\mathcal{F}_\mathcal{T}$ is the tidal oscillatory salt flux. With this decomposition, the net outflow current u_o is the time average of the volume transport divided by the time-averaged cross-sectional area. Therefore, Q_f includes the volume transport resulting from correlations between tidal currents and fluctuations in the cross-sectional area (Hunkins 1981; Jay 1991; Bowen and Geyer 2003).

4. Data and processing

The data used in this analysis were collected in the Hudson River estuary (Fig. 1) in the spring of 2002. A cross-channel array of moored acoustic Doppler current profilers (ADCPs) and temperature, conductivity, and pressure sensors (Fig. 2) was deployed from 23 April to 5 June (43 days) at about 23 km north of the Battery at the southern tip of Manhattan Island (Fig. 1). At this location, the channel is approximately 1.6 km wide and 15.5 m deep at the thalweg. The ADCPs pinged every 3 s and recorded average currents every 15 min. The pressure sensors recorded average pressure every 5 min, and the temperature and conductivity sensors sampled once every 5 min.

High-resolution shipboard ADCP and conductivity, temperature, and depth (CTD) surveys were obtained at the cross-channel study site over two semidiurnal periods—once during neap tidal conditions on 8 May and again during spring tidal conditions on 24 May. Cross-channel ADCP surveys were made once every 15 min and CTD surveys were made every 30 min (every other river crossing). A temporal gap of 1.3 h occurred during the 8 May survey because of equipment malfunction.

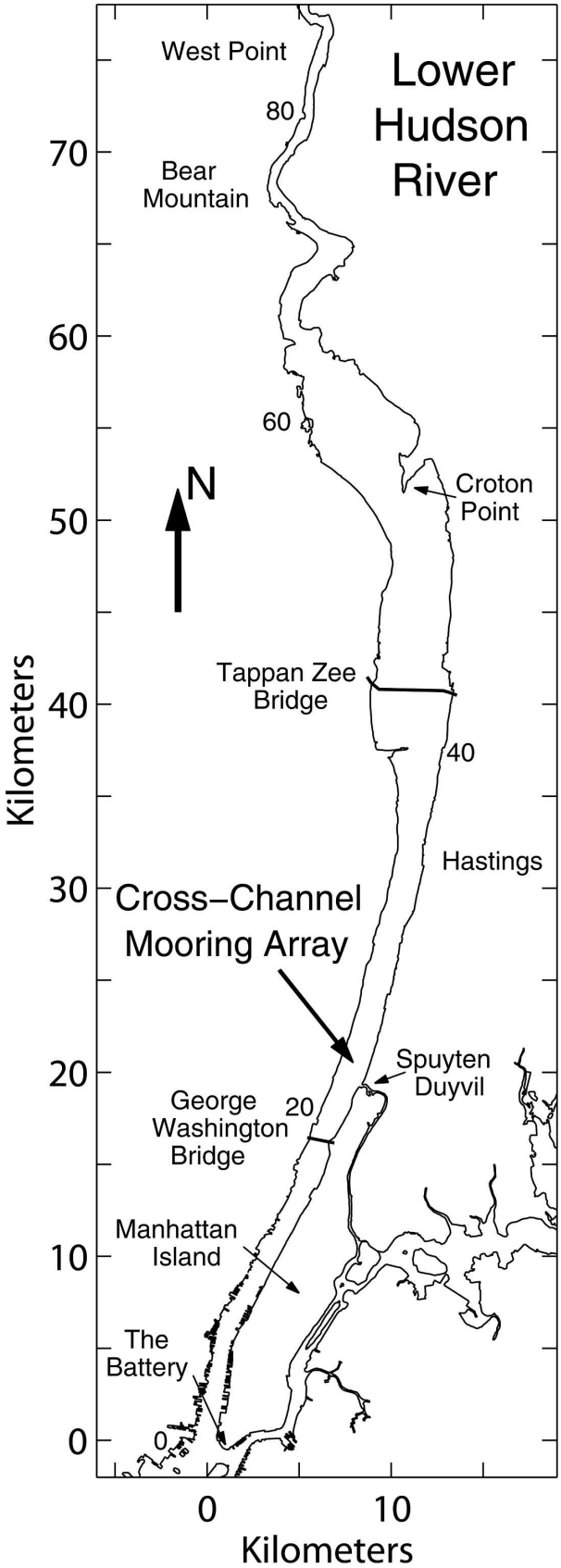

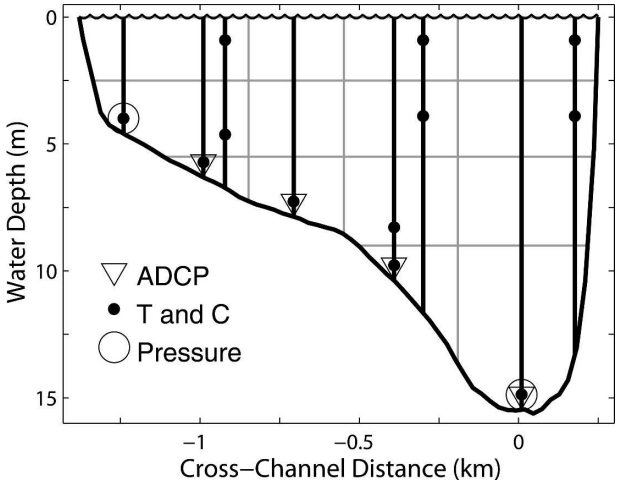

FIG. 2. Cross-sectional profile of the Hudson River at the location of the cross-channel mooring array showing the locations of moorings and instruments. The gray lines mark the borders of the 14 regions used to decompose the salt flux. The western side of the channel is on the left side of the figure.

In addition to the cross-channel sampling at the study site, hydrographic surveys along the thalweg of the estuary were obtained on nine occasions during the field study. These surveys took 2–4 h to complete and along-channel resolution was about 1 km. All of these surveys covered the region from the study site to the landward extent of the salinity intrusion ($S < 1$ psu), allowing us to estimate the total salt content within the estuary landward of the cross section where salt fluxes were calculated.

The data from each of the shipboard, hydrographic, and ADCP surveys were objectively mapped onto the λ–σ-coordinate system (4) with 25 uniformly spaced grid points in the cross-channel direction and 25 grid points in the vertical. For grid points not covered by the shipboard transects, S and u were extrapolated so that complete cross sections of these quantities were obtained. For S, the near-bottom and near-surface data were fitted to a parabola and the vertical gradient of S at the surface and bottom boundaries was forced to be zero.

Near the bottom of the water column, currents were extrapolated by fitting the near-bottom ADCP data to a log-layer profile,

←

FIG. 1. Map of the lower Hudson River showing the location of the cross-channel mooring array, approximately 23 river kilometers north of the Battery at the southern tip of Manhattan Island. The numbers along the river indicate river kilometers from the Battery.

TABLE 1. Deviations between instantaneous volume transport and instantaneous, cross-sectionally integrated salt flux estimated using the moored instrument array and the tidal cycle shipboard surveys during neap (8 May) and spring (24 May) tidal conditions.

	Neap (8 May)			Spring (24 May)		
	Tidal amplitude	Mean Δ*	Rms Δ**	Tidal amplitude	Mean Δ	Rms Δ
Transport ($m^3 s^{-1}$)	0.98×10^4	76	210	1.4×10^4	−15	250
Salt flux ($kg s^{-1}$)	0.75×10^5	−230	4.7×10^3	1.3×10^5	−610	3.7×10^3

* Tidal-averaged deviation between the moored and shipboard estimates over the tidal cycle survey.
** Rms deviation between the moored and shipboard estimates over the tidal cycle survey.

$$u(z + h) = \frac{u^*}{\kappa} \ln\left(\frac{z + h}{z_o}\right), \tag{10}$$

where κ is the von Kármán constant, and the roughness length z_o was set to 0.067 m. Currents were extrapolated over the upper 1.4 m of the water column that were not covered by the shipboard ADCP by fitting the near-surface data to a parabola and imposing the vertical shear be zero at the surface.

Efforts were made to cover as much of the cross section as possible with these surveys. For S, extrapolation was typically required for about 15% of the total area, predominantly in a region 1–2 m above the bottom. For u, extrapolation was typically required for 24% of the total area near the surface because of blanking distance constraints, and near the bottom because of sidelobe contamination.

The cross-sectionally gridded time series of u and S were then linearly interpolated onto a uniform time grid with 48 points (roughly the temporal resolution of the ADCP sampling and twice the resolution of the CTD sampling) and over one semidiurnal period (12.42 h). The salt flux and its components were computed according to (5)–(9). However, to reduce the contamination of diurnal tide variance in the subtidal components, values for Q_f and S_o were obtained from the moored observations (see below).

To estimate $\mathcal{F}_S$ and its various components using the mooring array, we decomposed the cross section into 14 subregions (Fig. 2), attempting to maximize spatial resolution, given the limited spatial coverage of the moored sensors. The cross section was divided laterally into four sections, separated by the midpoints between the four ADCPs. Four vertical levels were set by the locations of the temperature/conductivity sensors. The subregions were stretched vertically with tidal and subtidal sea level fluctuations in a manner consistent with the σ-coordinate system described in the previous section. For each of the subregions, referred to by the subscript i, time series of the area A_i, the area-averaged, along-channel current u_i, and the area-averaged salinity S_i were calculated. We estimated the salt flux and its components by

$$\mathcal{F}_S = \left\langle \sum_{i=1}^{14} u_i S_i A_i \right\rangle, \tag{11}$$

$$Q_f = \left\langle \sum_{i=1}^{14} u_i A_i \right\rangle, \quad S_o = \frac{1}{A_o} \left\langle \sum_{i=1}^{14} S_i A_i \right\rangle, \tag{12}$$

$$u_{\varepsilon_i} = \left\langle \frac{h_i + \xi}{h_i} u_i \right\rangle - \frac{1}{A_o} Q_f, \quad S_{\varepsilon_i} = \left\langle \frac{h_i + \xi}{h_i} S_i \right\rangle - S_o, \tag{13}$$

$$u_{\mathcal{T}_i} = u_i - u_{\varepsilon_i} - \frac{1}{A_o} Q_f, \quad \text{and} \quad S_{\mathcal{T}_i} = S_i - S_{\varepsilon_i} - S_o, \tag{14}$$

where h_i is the mean water depth at the location of the ADCP used to obtain the currents for a particular subregion.

To estimate u_i, current profiles from the four moored ADCPs were first extrapolated to the surface and the bottom in the same manner as that for the shipboard ADCP data. Over the breadth of the subregions covered by a particular ADCP, the vertical current structure was assumed to have the same shape as that measured at the location of the ADCP and was stretched or compressed to match the local depth. Using these methods to extrapolate the current structure across all subregions, the current was then averaged over each subregion to obtain u_i. The independent estimates of the instantaneous volume transport from the shipboard and moored measurements compare well. The root-mean-square (rms) deviation between the two estimates for the two semidiurnal cycles sampled during shipboard surveys was about 230 $m^3 s^{-1}$, or 2% of the amplitude of the tidal volume transport (Table 1). The deviation, averaged over a semidiurnal cycle, was <10% of the average subtidal transport over the entire 43-day time series.

The average salinity for each subregion was estimated by taking a weighted average of salinity calculated from one to four temperature and conductivity sensors in the vicinity of a particular subregion. Initially, the time-independent weights were based on proximity to the centroid of a subregion. These weights

were then refined to minimize the deviations from the instantaneous salt fluxes estimated from the shipboard measurements and the moored time series. We found that the instantaneous salt flux, estimated from the moored time series, was most sensitive to changes in the vertical distribution of the weighting than to changes in the horizontal distribution of the weighting. After optimal weights were chosen, the rms deviation between the shipboard and moored estimates of the instantaneous salt flux was about 4% of the amplitude of the tidally varying salt flux (Table 1), and the semidiurnal average deviation was <2% of the amplitude of $\mathcal{F}_S$. The tidal-averaged deviations provide an estimate of the uncertainty in $\mathcal{F}_S$ from the moored measurements ($\sim$500 kg s^{-1}).

Total salt content north of the cross-sectional study site was calculated using the along-channel hydrographic surveys. Individual casts were first advected in the along-channel direction either forward or backward in time, using area-averaged tidal currents estimated at the cross section, to minimize the effect of tidal advection during the period of a survey and to bring the casts from each survey to a common time in the tidal cycle (either at maximum flood or ebb, i.e., the midpoint of a tidal excursion). The profiles of S from these advected casts were then objectively mapped onto a uniform grid and the volume integral of S from the cross-sectional study site to the northern extent of the salinity intrusion was calculated using the local bathymetry of the channel and assuming that the vertical structure of S did not vary in the cross-channel direction.

5. Decomposition of *u* and *S*

a. Tides, Q_f and S_o

During the 43-day mooring deployment, the semidiurnal tidal current amplitude varied from about 0.5 to 1 m s^{-1} (Fig. 3a). Spring tides occurred on three occasions during this period, centered on days 116, 132, and 145, with the first and last being stronger than the middle. Three neap tides were centered on days 124, 138, and 154, with the last one being the weakest (apogean neap).

The net outflow Q_f was calculated from the mooring array, using (12), and was compared with data from the U.S. Geological Survey (USGS), which operates a streamflow gauge at the Green Island Dam, about 250 km north of the Battery (Fig. 3b). The Green Island Dam data were multiplied by a factor of 1.6 to account for the fraction of the Hudson River watershed south of the dam. The two time series reveal the same low-frequency features. Prior to day 132, Q_f was about 500 m^3 s^{-1} (oceanward). On day 133 (13 May), a storm

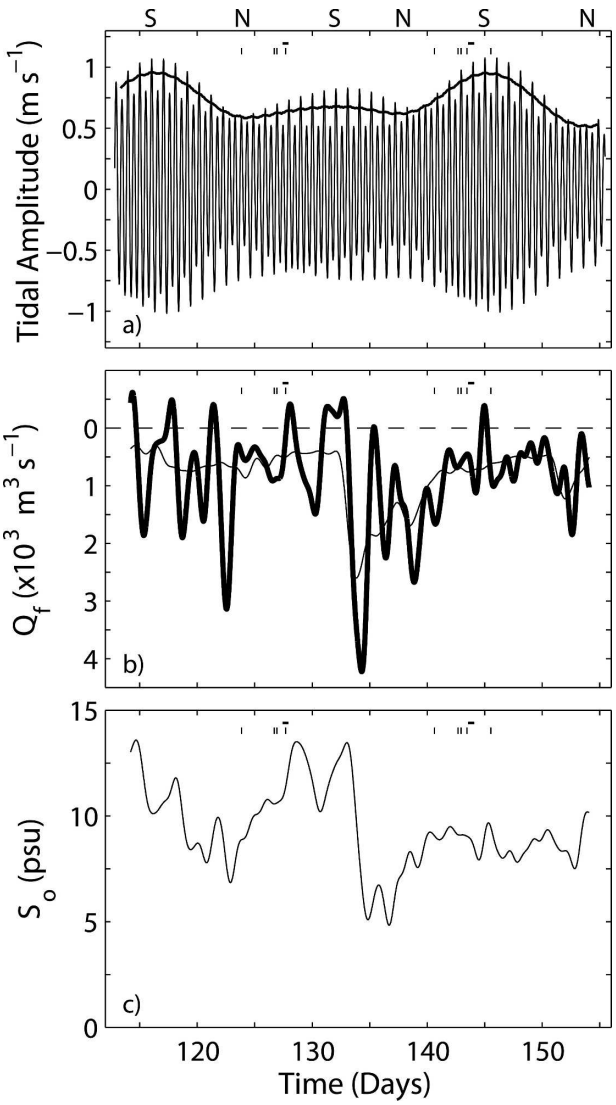

FIG. 3. (a) Time series of the area-averaged, harmonically filtered tidal currents at the cross-channel study site. The thick line shows the amplitude of the semidiurnal tide. The letters "S" and "N" at the top of the panel indicate peak spring and neap tidal conditions, respectively. (b) The net outflow Q_f, calculated using the ADCP data at the cross-channel mooring array (thick line) and from the USGS streamflow gauge at the Green Island Dam (multiplied by 1.6; thin line). Positive values indicate oceanward flow. (c) The S_o at the cross-channel mooring array. The short vertical lines at the top of each panel indicate the times when along-estuary hydrographic surveys were conducted. The two short horizontal lines indicate the periods when high-resolution, tidal cycle, shipboard hydrographic, and ADCP cross-channel surveys were conducted.

event occurred and Q_f rose to a peak value of over 4000 m^3 s^{-1}. Over the next 11 days, Q_f decreased to nearly prestorm values. This range of Q_f represents strong to moderate flow conditions for the Hudson, for which Q_f can range from 100 m^3 s^{-1} during summer and

early autumn drought conditions to >5000 $m^3 s^{-1}$ during the spring freshet (Abood 1974).

Large 3–5-day period oscillations of Q_f were observed at the study site, but were not apparent in the stream gauge record. These oscillations were also apparent in the sea level records and were likely driven by sea level pressure gradients resulting from local atmospheric forcing and nonlocally driven sea level fluctuations at the estuary mouth (Garvine 1985). These oscillations draw salt in and out of the estuary on a 3–5-day time scale, and can cause Q_f to be landward for brief periods of time. However, these oscillations are probably not important to the long-term salt balance in the estuary Bowen (2000).

The area-averaged subtidal salinity at the cross section S_o, calculated using (12), varied between 5 and 14 psu. As we will show, the fluctuations in S_o track the variations in the length of the salinity intrusion and the total salt content north of the study site.

b. u_ε and S_ε

The cross-channel structure of the estuarine exchange flow u_ε varied significantly over the spring–neap cycle (Fig. 4). On 8 May, during a neap tide, the oceanward flow exceeded 45 cm s^{-1} at the surface and the core of the landward flow exceeded 30 cm s^{-1} at middepth and centered on the thalweg. Strong vertical shear occurred between 3 and 6 m below the surface, with isotachs tilted slightly downward to the east.

During spring tide conditions on 24 May, u_ε was weaker in comparison with currents during neap tides, with a maximum landward flow of 15 cm s^{-1} and a maximum oceanward flow of 22 cm s^{-1}. The circulation had significant lateral variations, with maximum oceanward flow at the flanks, particularly on the eastern flank, and weak currents at the surface in the middle of the channel.

To compare the estimates of u_ε from the shipboard and moored measurements, we average the shipboard estimates over the subregions used for the moored data (Figs. 4c and 4c). In principle, the area-averaged shipboard estimate should be identical to the moored estimate. The basic structure of u_ε is captured by both estimates, for example, the spring/neap variation in the strength of u_ε is apparent in both, as well as the tendency for the oceanward flow to be enhanced at the flanks during spring tides. However, the strength of u_ε from the shipboard measurements is stronger during neap tides (cf. Figs. 4c and 4e) and weaker during spring tides (cf. Figs. 4d and 4f), in comparison with the moored estimate. The shipboard estimate of exchange transport (landward transport minus oceanward transport) is 32% greater than the moored estimate during the neap tide survey and 36% less than the moored estimate during the spring tide survey. This suggests that spring/neap variations in the amplitude of u_ε are somewhat muted in the estimate from moored observations.

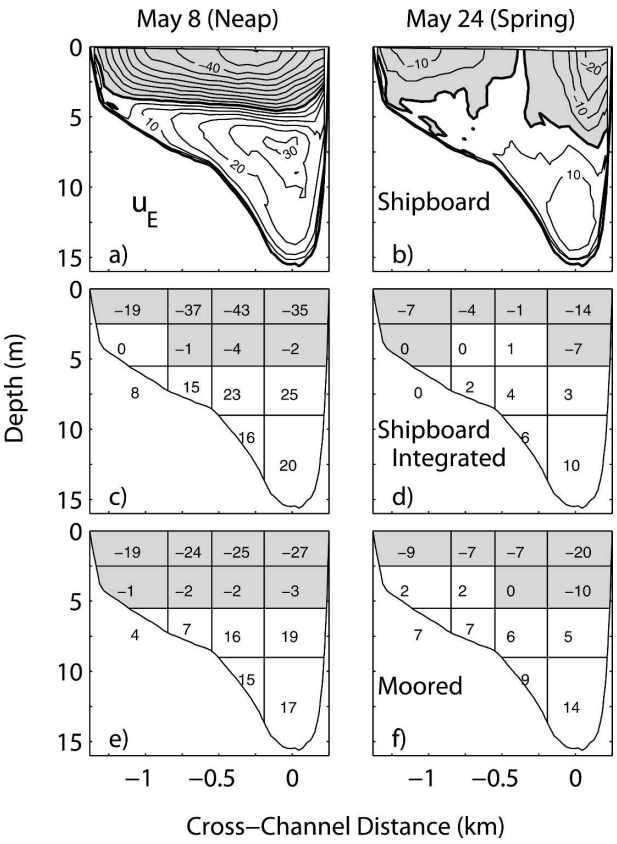

FIG. 4. Cross-channel profiles of the subtidal estuarine circulation u_ε during (left) neap and (right) spring tidal conditions. The upper four panels were calculated from the cross-channel, tidal cycle shipboard surveys. (a), (b) The contour interval is 5 cm s^{-1}, with 0 cm s^{-1} contoured with a thick line. (c), (d) The u_ε from the shipboard surveys was averaged over the subregions used for the moored observations. The values of u_ε (cm s^{-1}) are indicated for each subregion. (e), (f) The u_ε was calculated from the cross-channel mooring array over the same semidiurnal time period as the shipboard surveys. For all panels, oceanward (negative) currents are shaded gray.

Over the 43-day period of the study, the exchange flow (difference between surface and bottom flow; Fig. 5a) varied by roughly a factor of 2 over the spring–neap cycle. However, these spring/neap variations were confounded by the influence of the varying Q_f on the exchange flow. Note, in particular, the strong estuarine exchange flow that occurred on day 138 during a neap tide when Q_f was comparatively strong ($\approx$1500 $m^3 s^{-1}$) relative to the other two neaps in the record.

The estuarine salinity S_ε varied dramatically over the

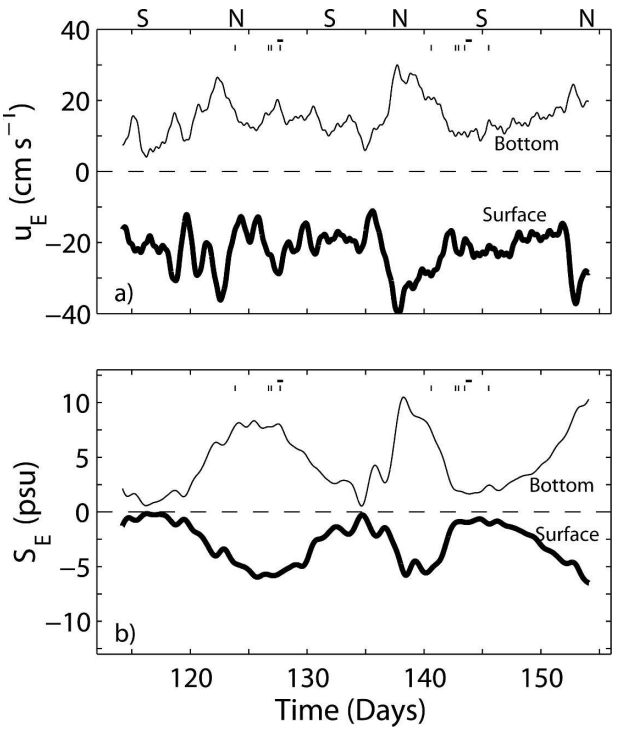

FIG. 5. Time series of (a) u_ε and (b) S_ε from the cross-shore mooring array. Surface values (thick line) are from the upper easternmost subregion and bottom values (thin line) are from the bottommost subregion.

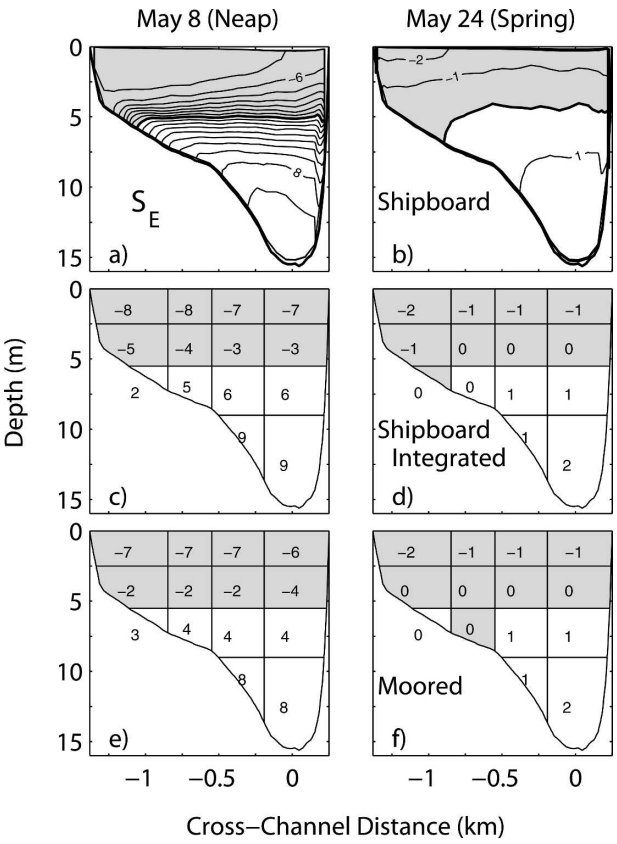

FIG. 6. Similar to Fig. 4, showing the cross-channel structure of S_ε, the subtidal, cross-sectionally varying salinity with the cross-sectional mean S_o removed [see Eq. (7)]. (a), (b) The contour interval is 1 psu. Regions with negative S_ε are shaded gray.

spring–neap cycle with order of magnitude changes in stratification (Figs. 5b and 6). The top-to-bottom salinity difference ranged from 15–20 psu during neap tides to 1–3 psu during spring tides. During the neap tide of 8 May (Figs. 6a and 6c), isohalines at the surface were tilted upward to the east, with the freshest water on the western side of the channel. A sharp halocline was present between 3 and 6 m, and isohalines were tilted downward to the east below the halocline. Consequently, the halocline was sharpest to the west and thickened to the east. During the spring tide on 24 May, the top-to-bottom salinity difference in S_ε was only 3 psu. Like the neap tide, freshest water occurred on the western flank of the channel. The spatial structure and the amplitude of S_ε is similar for the estimates from the shipboard observations and the moored observations (Figs. 6c–f).

For both cross-channel shipboard surveys, the vertical shear in u_ε was not in thermal wind balance with the tilting isohalines, suggesting that secondary flows and internal stresses are significant contributors to the cross-channel momentum balance (Lerczak and Geyer 2004). The lateral spreading of the halocline from west to east during neap tides is also consistent with the influence of secondary circulation, with middepth water being advected laterally from west to east (Lerczak and Geyer 2004).

6. Total salt flux $\mathcal{F}_S$

The instantaneous salt flux (Fig. 7a) varied in amplitude from about 15×10^4 kg s^{-1} during springs to about 7×10^4 kg s^{-1} during neaps. The tidally averaged total salt flux $\mathcal{F}_S$ was about an order of magnitude less than the instantaneous salt flux, and varied on several time scales (Fig. 7b). The large fluctuations at periods of 3–5 days were due to oscillations in Q_f (Fig. 3b) at the study site. During the storm on day 133, $\mathcal{F}_S$ had a maximum oceanward value of 3.2×10^4 kg s^{-1}. Over the spring–neap cycle, $\mathcal{F}_S$ was generally oceanward (negative) during springs and landward during neaps. This is most apparent when $\mathcal{F}_S$ is low passed to remove the 3–5-day oscillations (Fig. 3b, thin line).

7. Salt flux decomposition

The decomposition of $\mathcal{F}_S$ reveals that steady shear dispersion $\mathcal{F}_\varepsilon$ varied in amplitude by over an order of

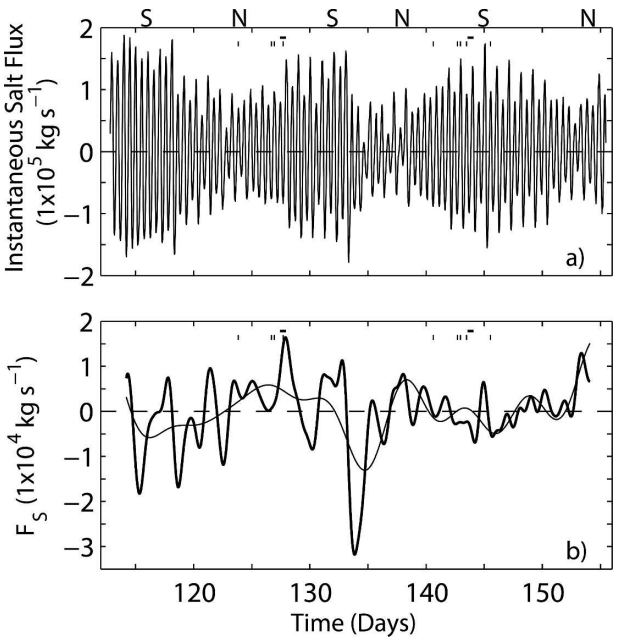

FIG. 7. (a) Instantaneous salt flux and (b) tidally averaged salt flux $\mathcal{F}_S$ at the cross-channel mooring array (thick line). The thin line shows the total salt flux, low-pass filtered to removed fluctuations with periods shorter than 5 days. Note that the y-axis scales are different for the two panels. A negative value indicates an oceanward salt flux.

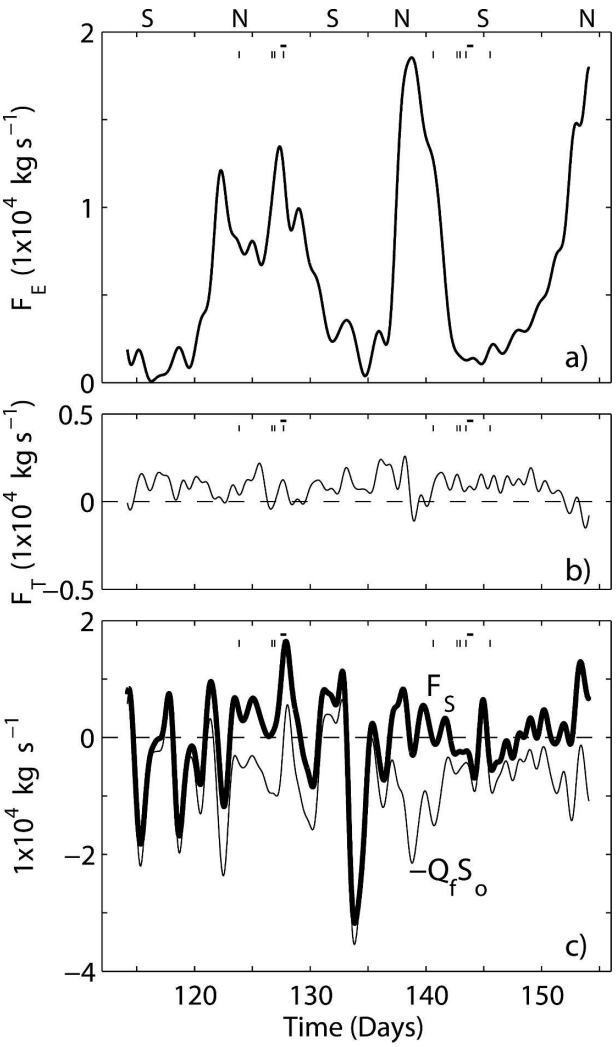

FIG. 8. (a) Salt flux resulting from steady, subtidal shear dispersion $\mathcal{F}_\varepsilon$. (b) Salt flux resulting from tidal oscillatory dispersion $\mathcal{F}_\mathcal{T}$. (c) Total salt flux $\mathcal{F}_S$ (thick line), and oceanward advective salt flux resulting from the net outflow $-Q_f S_o$ (thin line). Fluxes were calculated from the cross-channel mooring array. A positive flux is landward. The y-axis scale is the same for (a) and (b), but is compressed for (c).

magnitude over the spring–neap cycle (Fig. 8a). During neap tides, landward $\mathcal{F}_\varepsilon$ exceeded the oceanward advective flux ($-Q_f S_o$), with peak values of 1.8×10^4 kg s^{-1} during the two neap tides centered on days 138 and 154. During spring tides, $\mathcal{F}_\varepsilon$ was negligible in comparison with the advective salt flux. The order of magnitude fluctuations in stratification S_ε (Fig. 5b) over a spring–neap cycle were the principal cause of the spring–neap variations in $\mathcal{F}_\varepsilon$. The factor-of-2 spring–neap variations in u_ε (Fig. 5a) also contributed to the variability in $\mathcal{F}_\varepsilon$, but to a smaller degree.

In contrast, the tidal oscillatory salt flux $\mathcal{F}_\mathcal{T}$ was comparatively small throughout the 43-day time series (Fig. 8b). Averaged over the entire time series, $\overline{\mathcal{F}_\mathcal{T}}$ was 800 kg s^{-1}, while $\overline{\mathcal{F}_\varepsilon}$ was 6000 kg s^{-1} ($\overline{\mathcal{F}_\mathcal{T}}/\overline{\mathcal{F}_\varepsilon} \approx 0.13$). Averaging only during periods of neap tide conditions, $\overline{\mathcal{F}_\mathcal{T}}/\overline{\mathcal{F}_\varepsilon} \approx 0.03$. During spring tides, $\mathcal{F}_\varepsilon$ and $\mathcal{F}_\mathcal{T}$ were comparable in magnitude, but both were small in comparison with $-Q_f S_o$.

There is some suggestion that the amplitude of $\mathcal{F}_\mathcal{T}$ varied over a spring–neap cycle, being largest during spring tides and smallest (and possibly countergradient) during neap tides. This is particularly evident during the neap tides centered on days 138 and 154, when stratification was strongest (Fig. 5b). The reason for this spring/neap variation in $\mathcal{F}_\mathcal{T}$ will be discussed in section 7b.

Integrating (1) along the estuary axis, from the cross section where the salt flux is estimated to an upriver location beyond the extent of the salinity intrusion, gives an equation for the time rate of change of the salt content in the estuary, landward of the cross section,

$$\frac{\partial M_S}{\partial t} = -Q_f S_o - A_o(x)K(x)\frac{\partial S_o}{\partial x} = -Q_f S_o + \mathcal{F}_\varepsilon + \mathcal{F}_\mathcal{T}, \tag{15}$$

where M_S is the mass of salt landward of the cross section. During the period studied here, the salt balance

is unsteady, as indicated by the time derivative of salt content being comparable in amplitude to the individual flux terms (Fig. 8c),

$$\left|\frac{\partial M_S}{\partial t}\right| \sim |\mathcal{F}_\varepsilon| \sim |Q_f S_o|. \tag{16}$$

During spring tides, $\partial M_S/\partial t$ is predominantly balanced by the advective salt flux, and salt leaves the estuary. During neap tides, $\mathcal{F}_\varepsilon$ exceeds $Q_f S_o$ and salt enters the estuary.

Large 3–5-day period oscillations are apparent in the advective salt flux (Fig. 8c), which are principally due to variability in the net outflow (Fig. 3b). In contrast, these oscillations do not occur in $\mathcal{F}_\varepsilon$, because the estuarine circulation and the changes in stratification occur mainly at the spring–neap period, and are not strongly affected by the barotropic advective motions associated with the 3–5-day period oscillations.

a. Spatial structure of $\mathcal{F}_\varepsilon$

We contrast the cross-channel structure of $\mathcal{F}_\varepsilon$ during neap and spring tides by averaging the value of $\mathcal{F}_\varepsilon$ from the individual subregions over 2-day periods centered on the three neap tides and the three spring tides observed during the mooring deployment (Fig. 9). The structure of $\mathcal{F}_\varepsilon$ was also obtained from the cross-channel shipboard surveys for the single neap and spring semidiurnal cycles covered by those surveys.

During both spring and neap tides, $\mathcal{F}_\varepsilon$ is up estuary over most of the cross section, with the magnitude being an order of magnitude larger during neap than spring tides. Small areas of weak countergradient (oceanward) fluxes occurred at the halocline during neap tides (Figs. 9a and 9c) and on the western and eastern flanks and in the center of the channel during spring tides (Figs. 9b and 9d). These regions of countergradient flux are likely due to the lateral advection of salt by the secondary circulation.

Various methods for decomposing u_ε and S_ε have been proposed in order to determine the relative importance of vertical and lateral shear dispersion to the total steady shear dispersion salt flux $\mathcal{F}_\varepsilon$ (Rattray and Dworski 1980; Kay et al. 1996). One method is to estimate the vertical steady shear dispersion salt flux $\mathcal{F}_{\varepsilon V}$ by laterally averaging both u_ε and S_ε before integrating their product over the cross section. In so doing, only vertical variations in u_ε and S_ε contribute to the salt flux. Similarly, lateral steady shear dispersion salt flux $\mathcal{F}_{\varepsilon L}$ is estimated by vertically averaging u_ε and S_ε prior to integrating.

We adopt this approach for computing $\mathcal{F}_{\varepsilon V}$ and $\mathcal{F}_{\varepsilon L}$ and compare their relative amplitudes. Because water depth is usually not uniform over an estuary cross section, decompositions of u_ε and S_ε into laterally averaged, vertically varying and vertically averaged, laterally varying components are not orthogonal, and lateral and vertical contributions cannot be uniquely distinguished. As a consequence, $\mathcal{F}_\varepsilon \neq \mathcal{F}_{\varepsilon V} + \mathcal{F}_{\varepsilon L}$. However, this decomposition approach is useful when one steady shear dispersion mechanism dominates over the other. When the two mechanisms are comparable in amplitude, interpretation is difficult.

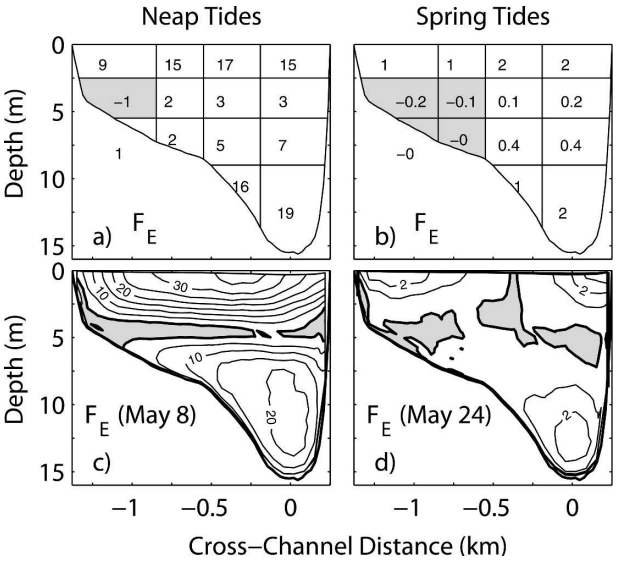

FIG. 9. Spatial structure of the steady dispersive salt flux $\mathcal{F}_\varepsilon$ during (a), (c) neap and (b), (d) spring tidal conditions. In (a) and (b), $\mathcal{F}_\varepsilon$ was calculated from the cross-channel mooring array and averaged over three 2-day periods centered on the (a) neap and (b) spring tidal conditions (Fig. 3a). Values of $\mathcal{F}_\varepsilon$ for each subregion (normalized by the tidally averaged area of that subregion) are expressed in units of 10^{-1} kg m^{-2} s^{-1}. In (c) and (d), $\mathcal{F}_\varepsilon$ was calculated from the cross-channel, tidal cycle shipboard surveys during neap (8 May) and spring (24 May) tidal conditions. The contour interval is 5×10^{-1} kg m^{-2} s^{-1} in (c) and 2×10^{-1} kg m^{-2}s^{-1} in (d). Areas with countergradient (oceanward) salt flux are shaded gray.

In this study, it is apparent that vertical shear dispersion dominates over lateral shear dispersion (Fig. 10). The decomposition suggests that $\mathcal{F}_{\varepsilon L}$ accounts for only about 10% of $\mathcal{F}_\varepsilon$.

b. Spatial structure of $\mathcal{F}_\mathcal{T}$

The cross-channel structure of the tidal oscillatory salt flux (Fig. 11) was determined in the same manner as that for steady shear dispersion. While the cross-channel integral of the tidal oscillatory salt flux is small relative to $|\mathcal{F}_S|$, spatial patterns are apparent, which suggest different mechanisms at work during spring and neap tides. During spring tides (Figs. 11b and 11d), the

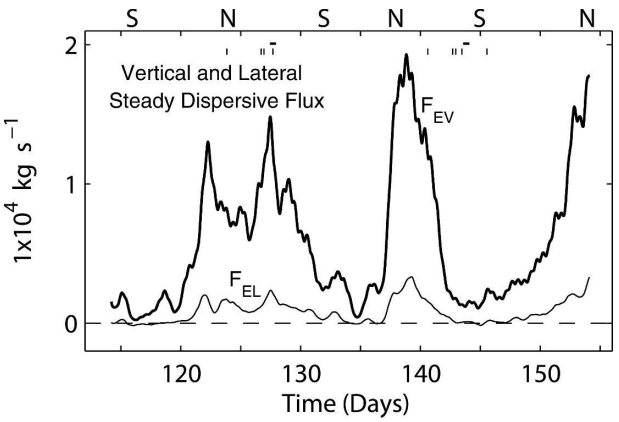

FIG. 10. Vertical and lateral steady shear dispersion flux calculated from the cross-channel mooring array. For $\mathcal{F}_{\varepsilon V}$ (thick line), lateral variability in u_ε and S_ε was averaged over before the flux was calculated. For $\mathcal{F}_{\varepsilon L}$ (thin line), vertical variability in u_ε and S_ε was averaged first.

spatial structure is consistent with tidal oscillatory shear dispersion. The flux near the bottom boundary layer is countergradient (negative) as a consequence of tidal currents near the bottom leading currents higher up in the water column (Larsen 1977; Ou et al. 2000). The salt flux increases toward the surface where the tidal currents are stronger, and the area-integrated value is downgradient (positive). The weak countergradient flux near the surface on the western side of the channel is likely due to an interaction between the tidally varying secondary circulation, lateral salinity gradients, and longitudinal tidal currents.

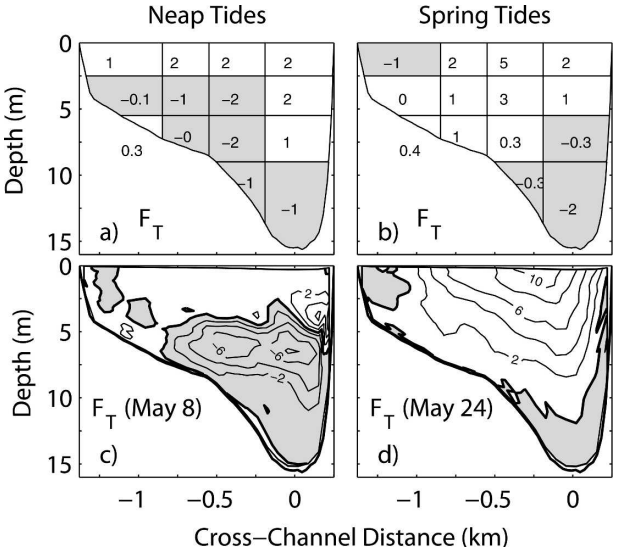

FIG. 11. Similar to Fig. 9, showing the spatial structure of the tidal oscillatory dispersion term $\mathcal{F}_{\mathcal{T}}$ during (a), (c) neap and (b), (d) spring tidal conditions. The contour interval in (c) and (d) is 2×10^{-1} kg m^{-2} s^{-1}.

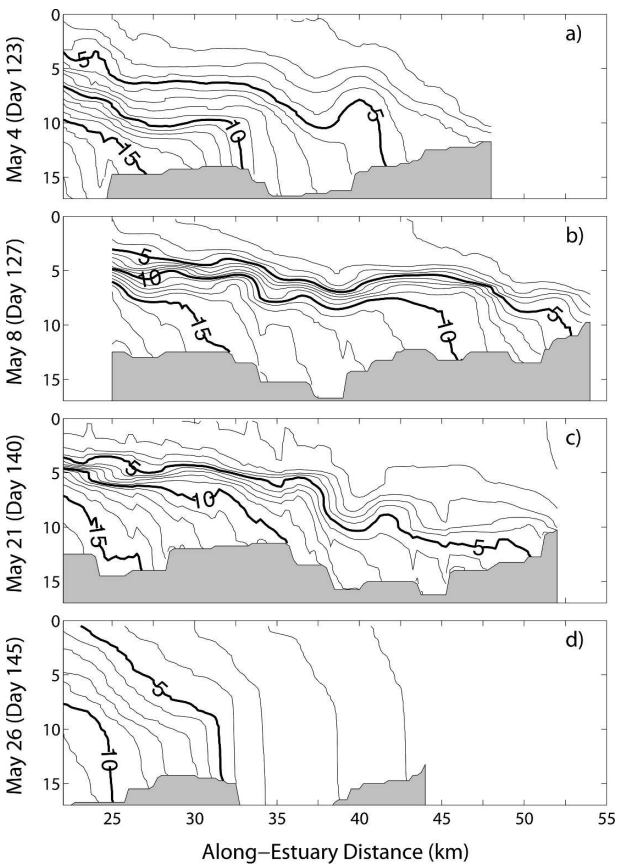

FIG. 12. Along-estuary salinity profiles obtained from shipboard hydrographic surveys. Individual casts were advected either forward or backward in time to minimize the effect of tidal advection and bring the casts to a common time in a tidal cycle.

During neap tides, the tidal oscillatory salt flux is positive near the surface and negative near the bottom, with a peak in countergradient (negative) flux near the depth of the halocline (Figs. 11a and 11c). This countergradient salt flux at the halocline is due to correlations between halocline depth and tidal currents. During the initial 2–3 h of flood tide, the halocline drops by about 2 m relative to its position over the rest of the tidal cycle. Consequently, midcolumn water was fresher during the flood than ebb, resulting in a negative tidal oscillatory salt flux at the halocline.

8. Along-estuary structure and salt content

In Fig. 12, we show the along-estuary structure of the salinity intrusion northward from the cross-channel mooring array to the landward extent of the salinity intrusion from four of the nine along-estuary hydrographic surveys. On 4 May (Fig. 12a), at the beginning of a neap tide, salt was beginning to enter the estuary

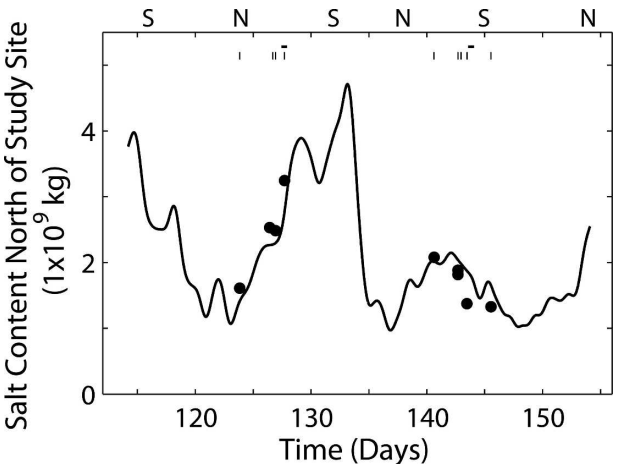

FIG. 13. Total salt content landward of the cross-channel mooring array. The filled circles are direct volume integral estimates from the nine along-estuary hydrographic surveys on seven different days. The curve is the time integral of $\mathcal{F}_S$ (Fig. 7b) with the constant of integration set so that the point estimates match the time integral on average.

(Fig. 7b), the water column was stratified, and the 5-psu isohaline reached to about 41 km upriver. Four days later (Fig. 12b), as salt continued to enter the estuary, the halocline sharpened, and the 5-psu isohaline moved about 12 km upriver to 53 km north of the Battery.

The survey on 21 May occurred during a neap tide about 7 days after the large freshwater pulse (Fig. 12c). The water column was stratified, salt was entering the estuary, and the 5-psu isohaline extended to 51 km. Five days later (Fig. 12d), the stratification was significantly reduced during a spring tide, and the 5-psu isohaline was driven about 20 km oceanward to 31 km north of the Battery, resulting from both oceanward advection and vertical mixing.

The volume-integrated salt content north of the study site, calculated from the nine along-estuary surveys (Fig. 13), ranged from 1.3 to 3.2 $\times$ 10^9 kg. The salt content was also estimated by integrating $\mathcal{F}_S$ in time. The constant of integration, that is, the salt content at the beginning of the field study, was estimated by minimizing the squared residual between the nine point estimates of salt content from the along-channel surveys and the values for those times obtained from the time integral of $\mathcal{F}_S$. Using an initial salt content of 3.1 $\times$ 10^9 kg for the time series, the rms difference between the point estimates and the time series was 1.4 $\times$ 10^8 kg, which is an order of magnitude smaller than the temporal variations in salt content.

This suggests that the two independent estimates properly represent time variations in salt content and lend confidence in the estimate of $\mathcal{F}_S$, despite the difficulties in calculating it that are outlined in the introduction. A bias in the estimate of $\mathcal{F}_S$ (if it is biased) must be small. For example, a bias of just 5% of the amplitude of $\mathcal{F}_S$ ($\sim$1000 kg s^{-1}, or twice the estimated uncertainty in $\mathcal{F}_S$ based on tidal-averaged deviations between moored and shipboard estimates; Table 1) would cause a linear increase (or decrease) in the estuarine salt content of 3.7 $\times$ 10^9 kg over the 43-day time series, or nearly twice the average salt content of the estuary over this period (Fig. 13). This is unlikely, because if there were such a bias, the salt content estimates based on $\mathcal{F}_S$ and the longitudinal hydrographic surveys would not compare well.

9. Discussion and conclusions

In the relatively straight reach of the Hudson River estuary studied here, the downgradient salt flux was dominated by steady shear dispersion and exhibited order of magnitude variations over the spring–neap cycle. The estuary was not in a steady state over the spring–neap cycle, that is, the advective and dispersive salt fluxes did not balance, and the magnitude of the time rate of change of salt content in the estuary was comparable to the magnitude of the individual flux terms. Unsteadiness in the salt balance has also been observed in other estuarine systems (Simpson et al. 2001; Banas et al. 2004).

During spring tides, the time rate of change of salt content was predominantly balanced by the oceanward advective salt flux, and salt was flushed out of the estuary. During neap tides, both the advective salt flux and the steady shear dispersion flux were dominant terms in the balance, but shear dispersion exceeded the advective flux, and salt entered the estuary. Tidal oscillatory salt flux was not a dominant term in the salt balance. Factor-of-4 variations of salt content occurred over the 43-day period of the study (Fig. 13) on both the spring–neap time scale and at the time scale of variations in Q_f, reflecting the rapid response time of the estuary during this period of moderate to high Q_f.

These results are consonant with those of Bowen and Geyer (2003), and we expand their conclusions by exploring the estuary's salt balance during a period of moderate to large freshwater discharge. A summer drought occurred in 1995, during most of the field study discussed by Bowen and Geyer (2003), with Q_f at a nearly constant value of 100 m^3 s^{-1}. The oceanward advective salt flux was nearly constant ($\sim$2000 kg s^{-1}), and steady shear dispersion was negligible except for pulses during the weakest (apogean) neap tides, when salt entered the estuary. During apogean neaps, maximum $\mathcal{F}_e$ was about 7500 kg s^{-1}, with a corresponding

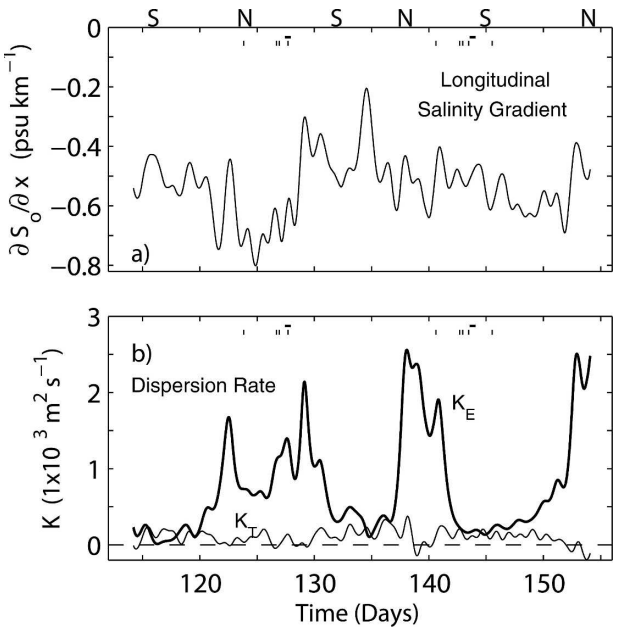

FIG. 14. (a) Longitudinal salinity gradient, estimated from the approximate cross-sectionally averaged salt balance $\partial\overline{S}/\partial t + \overline{U}\,\partial S_o/\partial x = 0$, where $\overline{S}$ and $\overline{U}$ are the cross-sectionally averaged instantaneous salinity and longitudinal current, respectively. (b) Longitudinal dispersion rate K resulting from the steady dispersive salt flux (thick line) and the tidal oscillatory flux (thin line).

maximum dispersion rate K estimated to be 2600 $m^2\,s^{-1}$. The time response of the salt content of the estuary over the spring–neap cycle was sluggish, with the total salt content varying by only 10% over the spring–neap cycle, reflecting the slow response time of the estuary during low-river flow conditions. The estuary responded rapidly to a freshwater pulse ($Q_f \sim 1500$ $m^3\,s^{-1}$) at the end of their survey, with the estuary reducing in length from about 100 to 65 km over about 5 days during the storm. This decrease in estuarine response time with an increase in Q_f is consistent with the theoretical study of Kranenburg (1986) and the numerical study of MacCready (1999).

During the period studied here, Q_f ranged from 500 to 3000 $m^3\,s^{-1}$ (after the 3–5-day oscillations were filtered out). The salinity intrusion was compressed (the maximum length was about 55 km) and was much more variable over the spring–neap cycle, in comparison with the estuary during the drought conditions observed by Bowen and Geyer (2003). Steady shear dispersive salt flux was large during all neap tides (not just apogean), with peak values of $\mathcal{F}_\varepsilon$ of about 1.8×10^4 kg s^{-1}. The corresponding dispersion rate K was as large as 2500 $m^2\,s^{-1}$ during neap tides (Fig. 14). Thus, maximum neap tide dispersion rates observed here were comparable to those observed by Bowen and Geyer (2003) during apogean neaps, despite the large differences in the longitudinal salinity gradients present during these two studies; $\partial S_o/\partial x$ was about 3 times larger here than during the study of Bowen and Geyer (2003).

This apparent lack of dependence of K on the longitudinal salinity gradient contradicts the prediction for the dispersion rate obtained from the steady-state estuarine model of Hansen and Rattray (1965) and Chatwin (1976), for which K_{HR} is proportional to the square $\partial S_o/\partial x$ [Eq. (2)]. Using a numerical model, Hetland and Geyer (2004) showed that, with spring/neap changes in vertical mixing, u_ε and S_ε are often not in a quasi steady state, even when the estuarine adjustment time scale ($\tau \sim 1$ to $6 \times LA_o/Q_f$, where L is the length of the estuary) is comparable to or smaller than the spring/neap time scale. Neither u_ε nor S_ε follow the scalings predicted by the model of Hansen and Rattray (1965) and Chatwin (1976). Here, we have shown that the salinity intrusion in the Hudson is not in a steady state over the spring–neap cycle. This provides further support for the conclusion that a steady-state model is not adequate for describing the variability of the salt flux over the spring–neap cycle in partially mixed estuaries.

Vertical steady shear dispersion resulting from the estuarine exchange flow dominated over lateral steady shear dispersion during both neap and spring tides. This was also observed by Hunkins (1981) in the Hudson River, Rattray and Dworski (1980) in the Southampton Water, and Hughes and Rattray (1980) in the Columbia River. Uncles et al. (1985) also observed a dominance of vertical steady shear dispersion over lateral steady shear dispersion in the Tamar estuary, except for the widest cross section studied, where $\mathcal{F}_{\varepsilon V}$ and $\mathcal{F}_{\varepsilon L}$ were found to be comparable in magnitude.

Tidal oscillatory salt flux $\mathcal{F}_\mathcal{T}$ was not a dominant term in the salt balance, but was found to vary in amplitude and spatial structure over the spring–neap cycle, in contrast to the findings of Bowen and Geyer (2003), who found the amplitude of $\mathcal{F}_\mathcal{T}$ to be independent of the spring–neap cycle. However, Bowen and Geyer (2003) did not have adequate lateral resolution to resolve the spatial structure of $\mathcal{F}_\mathcal{T}$. Here, $\mathcal{F}_\mathcal{T}$ was weakest, and at times negative, during neap tides. This was due to the countergradient tidal-pumping salt flux associated with correlations between the tidal currents and fluctuations of the halocline, perhaps resulting from a hydraulic response to bathymetric variations. This contrasts the downgradient tidal-pumping salt flux observed by Geyer and Nepf (1996) in the vicinity of a channel constriction in the Hudson River. This nonlocal salt flux, which probably results from a distortion of the estuarine exchange flow, apparently can be either counter-

gradient or downgradient (Dronkers and van de Kreeke 1986; Geyer and Nepf 1996) at different locations in an estuary, depending on proximity to bathymetric variations.

During spring tides, $\mathcal{F}_T$ was downgradient and dominated by oscillatory shear dispersion. The value of $\mathcal{F}_T$, averaged over the 4-day periods centered on the three spring tides, was 980 kg s^{-1}, corresponding to an average dispersion rate of 130 m^2 s^{-1} (Fig. 14b). While this value is small relative to the dispersion rate associated with steady shear dispersion, it is comparable to the theoretically expected maximum oscillatory shear dispersion rate [Eq. (3); $\max(K_{\mathrm{OSD}}) \approx 140$ m^2 s^{-1}; assuming $U_T = 1$ m s^{-1}].

To summarize, in this study we used an array of cross-channel moorings and shipboard surveys to study the salt balance in the Hudson River estuary and to determine the mechanisms that drive the landward salt flux over the spring–neap cycle in tidal forcing and under varying freshwater flow conditions. We show that steady vertical shear dispersion is the dominant mechanism driving the downgradient salt flux at that location. The study also reveals the inherent unsteadiness of the salt balance over the spring–neap cycle and over the time scale of fluctuations in Q_f. Long time series, such as these, show the variability in the amplitude and spatial structure of the downgradient salt flux resulting from changes in forcing and could be applied elsewhere to identify the range of flux mechanisms in a variety of estuarine classes.

Acknowledgments. This work was supported by National Science Foundation Grant OCE00-95972 and Hudson River Foundation Grant 005/03A. Author Lerczak received partial support from the Penzance Endowed Fund in Support of Assistant Scientists. We acknowledge the helpful comments provided by Steve Lentz, Neil Banas, and two anonymous reviewers.

REFERENCES

Abood, K. A., 1974: Circulation in the Hudson Estuary. *Ann. N.Y. Acad. Sci.,* **250,** 39–111.

Banas, N. S., B. M. Hickey, P. MacCready, and J. A. Newton, 2004: Dynamics of Willapa Bay, Washington: A highly unsteady, partially mixed estuary. *J. Phys. Oceanogr.,* **34,** 2413–2427.

Bowen, M. M., 2000: Mechanisms and variability of salt transport in partially-stratified estuaries. Ph.D. thesis, Joint Program in Physical Oceanography, Woods Hole Oceanographic Institution, 198 pp.

——, and W. R. Geyer, 2003: Salt transport and the time-dependent salt balance of a partially stratified estuary. *J. Geophys. Res.,* **108,** 3158, doi:10.1029/2001JC001231.

Chadwick, D. B., and J. L. Largier, 1999: The influence of tidal range on the exchange between San Diego Bay and the ocean. *J. Geophys. Res.,* **104,** 29 885–29 899.

Chatwin, P. C., 1976: Some remarks on the maintenance of the salinity distribution in estuaries. *Estuarine Coastal Mar. Sci.,* **4,** 555–566.

Dronkers, J., and J. van de Kreeke, 1986: Experimental determination of salt intrusion mechanisms in the Volkerak Estuary. *Neth. J. Sea Res.,* **20,** 1–19.

Fischer, H. B., 1972: Mass transport mechanisms in partially stratified estuaries. *J. Fluid Mech.,* **53,** 671–687.

——, E. J. List, R. C. Y. Koh, J. Imberger, and N. H. Brooks, 1979: *Mixing in Inland and Coastal Waters.* Academic Press, 483 pp.

Garvine, R. W., 1985: A simple model of estuarine subtidal fluctuations forced by local and remote wind stress. *J. Geophys. Res.,* **90,** 11 945–11 948.

Geyer, W. R., and R. P. Signell, 1992: A reassessment of the role of tidal dispersion in estuaries and bays. *Estuaries,* **15,** 97–108.

——, and H. M. Nepf, 1996: Tidal pumping of salt in a moderately stratified estuary. *Buoyancy Effects on Coastal and Estuarine Dynamics,* D. G. Aubrey and C. T. Friedrichs, Eds., Amer. Geophys. Union, 213–226.

Hansen, D. V., and M. Rattray Jr., 1965: Gravitational circulation in straits and estuaries. *J. Mar. Res.,* **23,** 104–122.

Harleman, D. R. F., and M. L. Thatcher, 1974: Longitudinal dispersion and unsteady salinity intrusion in estuaries. *Houille Blanche,* **1/2,** 25–33.

Hetland, R. D., and W. R. Geyer, 2004: An idealized study of the structure of long, partially mixed estuaries. *J. Phys. Oceanogr.,* **34,** 2677–2691.

Hughes, F. W., and M. Rattray Jr., 1980: Salt flux and mixing in the Columbia River estuary. *Estuarine Coastal Mar. Sci.,* **10,** 479–493.

Hunkins, K., 1981: Salt dispersion in the Hudson estuary. *J. Phys. Oceanogr.,* **11,** 729–738.

Jay, D. A., 1991: Estuarine salt conservation: A Lagrangian approach. *Estuarine Coastal Shelf Sci.,* **32,** 547–565.

——, and J. D. Smith, 1990: Circulation, density distribution and neap-spring transitions in the Columbia River Estuary. *Progress in Oceanography,* Vol. 25, Pergamon, 81–112.

——, and J. M. Musiak, 1996: Internal tidal asymmetry in channel flows: Origins and consequences. *Mixing in Estuaries and Coastal Seas,* C. Pattiaratchi, Ed., Amer. Geophys. Union, 211–249.

——, W. R. Geyer, R. J. Uncles, J. Vallino, J. Largier, and W. R. Boynton, 1997: A review of recent developments in estuarine scalar flux estimation. *Estuaries,* **20,** 262–280.

Kay, D. J., D. A. Jay, and J. D. Musiak, 1996: Salt transport calculations from acoustic Doppler current profiler (ADCP) and conductivity-temperature-depth (CTD) data: A methodological study. *Buoyancy Effects on Coastal and Estuarine Dynamics,* D. G. Aubrey and C. T. Friedrichs, Eds., Amer. Geophys. Union, 195–212.

Kranenburg, C., 1986: A time scale for long-term salt intrusion in well-mixed estuaries. *J. Phys. Oceanogr.,* **16,** 1329–1331.

Larsen, L. H., 1977: Dispersion of a passive contaminant in oscillatory fluid flows. *J. Phys. Oceanogr.,* **7,** 928–930.

Lerczak, J. A., and W. R. Geyer, 2004: Modeling the lateral circulation in straight, stratified estuaries. *J. Phys. Oceanogr.,* **34,** 1410–1428.

Li, C., and J. O'Donnell, 1997: Tidally driven residual circulation in shallow estuaries with lateral depth variation. *J. Geophys. Res.,* **102,** 27 915–27 929.

MacCready, R., 1999: Estuarine adjustment to changes in river flow and tidal mixing. *J. Phys. Oceanogr.,* **29,** 708–726.

Monismith, S. G., W. Kimmerer, J. R. Burau, and M. T. Stacey, 2002: Structure and flow-induced variability of the subtidal salinity field in northern San Francisco Bay. *J. Phys. Oceanogr.,* **32,** 3003–3019.

Okubo, A., 1967: The effect of shear in an oscillatory current on horizontal diffusion from an instantaneous source. *Int. J. Oceanol. Limnol.,* **1,** 194–204.

——, 1973: Effect of shoreline irregularities on streamwise dispersion in estuaries and other embayments. *Neth. J. Sea Res.,* **6,** 213–224.

Ou, H. W., C. M. Dong, and D. Chen, 2000: On the tide-induced property flux: Can it be locally countergradient? *J. Phys. Oceanogr.,* **30,** 1472–1477.

Rattray, M., and J. G. Dworski, 1980: Comparison of methods for analysis of the transverse and vertical circulation contributions to the longitudinal advective salt flux in estuaries. *Estuarine Coastal Mar. Sci.,* **11,** 515–536.

Simpson, J. H., R. Vermeil, and A. J. Souza, 2001: The salt fluxes in a tidally-energetic estuary. *Estuarine Coastal Shelf Sci.,* **52,** 131–142.

Smith, R., 1976: Longitudinal dispersion of a buoyant contaminant in a shallow channel. *J. Fluid Mech.,* **78,** 677–688.

Stacey, M. T., J. R. Burau, and S. G. Monismith, 2001: Creation of residual flows in a partially stratified estuary. *J. Geophys. Res.,* **106,** 17 013–17 037.

Stommel, H., and H. G. Farmer, 1952: On the nature of estuarine circulation, Part I. Woods Hole Oceanographic Institution Tech. Rep. 52–88, 131 pp.

Taylor, G. T., 1953: Dispersion of soluble matter in solvent flowing slowly through a tube. *Proc. Roy. Soc. London,* **A219,** 186–203.

Uncles, R. J., R. C. A. Elliot, and S. A. Weston, 1985: Dispersion of salt and suspended sediment in a partly mixed estuary. *Estuaries,* **8,** 256–269.

Zimmerman, J. T. F., 1986: The tidal whirlpool: A review of horizontal dispersion by tidal and residual currents. *Neth. J. Sea Res.,* **20,** 133–154.